Draft version January 23, 2026
Typeset using LaTeX **twocolumn** style in AASTeX7

Undermassive Hosts of $z = 4$–6 AGN from JWST/NIRCam Image Decomposition with CONGRESS, FRESCO, and JADES

Zheng Ma [1], Eiichi Egami [1], Yongda Zhu [1,*], Fengwu Sun [2], Jianwei Lyu [1], Junyu Zhang [1], Christopher N. A. Willmer [1], Andrew J. Bunker [3], Stefano Carniani [4], Emma Curtis-Lake [5], Ryan Hausen [6], Xihan Ji [7,8], Zhiyuan Ji [1,*], Ignas Juodžbalis [9], Roberto Maiolino [7,10,11], George H. Rieke [1], Pierluigi Rinaldi [12], Yang Sun [1], Sandro Tacchella [7,8], Hannah Übler [13] and Christina C. Williams [14]

[1] *Steward Observatory, University of Arizona, 933 North Cherry Avenue, Tucson, AZ 85721, USA*
[2] *Center for Astrophysics | Harvard & Smithsonian, 60 Garden St., Cambridge, MA 02138, USA*
[3] *Department of Physics, University of Oxford, Denys Wilkinson Building, Keble Road, Oxford OX1 3RH, UK*
[4] *Scuola Normale Superiore, Piazza dei Cavalieri 7, I-56126 Pisa, Italy*
[5] *Centre for Astrophysics Research, Department of Physics, Astronomy and Mathematics, University of Hertfordshire, Hatfield AL10 9AB, UK*
[6] *Department of Physics and Astronomy, The Johns Hopkins University, 3400 N. Charles Street, Baltimore, MD 21218, USA*
[7] *Kavli Institute for Cosmology, University of Cambridge, Madingley Road, Cambridge, CB3 0HA, UK*
[8] *Cavendish Laboratory, University of Cambridge, 19 JJ Thomson Avenue, Cambridge, CB3 0HE, UK*
[9] *Kavli Institute for Cosmology, University of Cambridge, Madingley Road, Cambridge, CB3 0HA, UK Cavendish Laboratory, University of Cambridge, 19 JJ Thomson Avenue, Cambridge, CB3 0HE, UK*
[10] *Cavendish Laboratory - Astrophysics Group, University of Cambridge, 19 JJ Thomson Avenue, Cambridge, CB3 0HE, UK*
[11] *Department of Physics and Astronomy, University College London, Gower Street, London WC1E 6BT, UK*
[12] *Space Telescope Science Institute, 3700 San Martin Dr., Baltimore, MD 21218, USA*
[13] *Max-Planck-Institut für extraterrestrische Physik (MPE), Gießenbachstraße 1, 85748 Garching, Germany*
[14] *NSF National Optical-Infrared Astronomy Research Laboratory, 950 North Cherry Avenue, Tucson, AZ 85719, USA*

ABSTRACT

In the local Universe, supermassive black hole (SMBH) masses strongly correlate with their host-galaxies' stellar masses (M_*), but galaxies hosting faint AGN recently found by JWST may deviate from this relation. To constrain the M_{BH}-M_* relation at high redshift, we performed AGN-host image decomposition for 17 low-luminosity AGN galaxies at $z \sim 4$–6 using NIRCam images in the JADES GOODS-N field. These sources are identified as AGNs from broad Hα emission lines detected by the CONGRESS and FRESCO surveys. We used GALFIT+MCMC to fit spatial profiles in 7 wide-band images and detected extended emission in 9 sources out of 17. The close spatial alignment between the extended components and the AGN centers indicates that this emission likely originates from the host galaxies. These sources are extended at 0.9–2.0 μm, suggesting significant host-galaxy light in the rest-frame UV. For the sources with the host detection, the stellar mass inferred based on image decomposition result can be 1-2 dex lower than the results without image decomposition. The BH-to-stellar mass ratio spans $M_{BH}/M_* \sim 0.01$–1.48, placing them well above the local M_{BH}–M_* relation. In contrast, the host-galaxy size–mass relation broadly agrees with previous measurements. Our results suggest that the host galaxies of these faint AGN are either genuinely under-massive compared to their black hole masses, or too compact to be spatially resolved.

Keywords: Active galactic nuclei (16), High-redshift galaxies (734), Galaxy morphology (582), Galaxy evolution (594)

1. INTRODUCTION

In the local universe, a well-established correlation exists between the masses of supermassive black holes (SMBHs) and host galaxy properties, such as bulge mass

Email: mazh@arizona.edu
* JASPER Scholar

and velocity dispersion (J. Magorrian et al. 1998; L. Ferrarese & D. Merritt 2000; K. Gebhardt et al. 2000; J. Kormendy & L. C. Ho 2013). These relationships are widely interpreted as evidence for the co-evolution of SMBHs and their host galaxies. Among these relations, one particularly interesting connection is the stellar mass – black hole mass (M_*–$M_{\rm BH}$) relation, which implies the growth of SMBHs and their hosts are intertwined. There are several theoretical models attempting to explain this correlation. For example, AGN can regulate host galaxy growth by heating or expelling its surrounding gas (R. S. Somerville et al. 2008; A. C. Fabian 2012; X. Fan et al. 2023). Other hypotheses suggest that the statistical effects of major and minor galaxy mergers naturally lead to a tight, linear correlation between SMBH mass and galaxy bulge mass, regardless of how the black holes were originally seeded, although simulations show that for massive galaxies ($M_* > 10^{10.9} M_\odot$), mergers are not the primary drivers of AGN activity (C. Y. Peng 2007; R. S. Sharma et al. 2024).

To understand the origin of the M_*–$M_{\rm BH}$ relation, it is necessary to examine this relation for black holes in their early stages. To derive this relation at high redshift, several studies have focused on AGN-host galaxy decompositions, particularly image decomposition techniques (e.g., X. Ding et al. 2023; M. Yue et al. 2024; Y. Harikane et al. 2023; C.-H. Chen et al. 2024; H. Yu et al. 2025; M. A. Stone et al. 2023), fitting AGN-galaxy images with a combination of a single Sérsic profile and a point source profile. However, observing this relation becomes increasingly challenging at high redshifts. Galaxies hosting AGN are typically more compact at these redshifts, with their stellar light often being outshined by the AGN, making it difficult to separate the host galaxy from the AGN component.

The James Webb Space Telescope (JWST) presents a unique opportunity to overcome these challenges with its high-resolution imaging and sensitivity in the near-infrared. In recent years, JWST has demonstrated its capability to identify UV-faint AGN-host galaxies at high redshift ($z > 5$) through the detection of broad Balmer emission lines (J. Matthee et al. 2024; R. Maiolino et al. 2024; I. Juodžbalis et al. 2025a; J. E. Greene et al. 2024; H. Übler et al. 2023; R. L. Larson et al. 2023; D. D. Kocevski et al. 2023; Y. Harikane et al. 2023; V. Kokorev et al. 2024). These UV-faint AGNs appear to be significantly more abundant than previously expected—their number density at $z \sim 5$ is measured to be one to two orders of magnitude higher than estimates based on extrapolations of the quasar UV luminosity function (J. Matthee et al. 2024; R. Maiolino et al. 2024; I. Juodžbalis et al. 2025a; Y. Harikane et al. 2023; D. D. Kocevski et al. 2023; J. E. Greene et al. 2024). These low-luminosity, broad-line AGN galaxies typically host moderate-mass black holes with masses in the range of 10^{6-8} $M_\odot$, derived from locally calibrated single-epoch methods or direct black hole mass measurement (J. Matthee et al. 2024; R. Maiolino et al. 2024; Y. Harikane et al. 2023; I. Juodžbalis et al. 2025b; S. Geris et al. 2026). In comparison, luminous quasars at similar redshifts are found to host black holes with masses of $\sim 10^{8-10} M_\odot$ (X. Fan et al. 2023; B. Trakhtenbrot et al. 2011). UV-faint AGNs therefore provide ideal laboratories for constraining host-galaxy properties and investigating the co-evolution of supermassive black holes and their hosts. First, their relatively low black hole masses compared to luminous quasars suggest that they represent an earlier stage of black hole growth. Second, their low AGN luminosities reduce host–AGN contrast, making it easier to detect and characterize the underlying host galaxies without being completely outshone by the AGN.

About 15 - 30% of broad-line AGN identified by JWST are "little red dots" (LRDs; J. Matthee et al. 2024; K. N. Hainline et al. 2025). Currently, there is no unified selection criterion for identifying these objects. Spectroscopically, they exhibit a distinctive "V-shaped" continuum, with a red slope in the rest-frame optical and a blue slope in the rest-frame UV (L. J. Furtak et al. 2024). Photometrically, they are characterized by their compact morphology in rest-frame UV and red colors (V. Kokorev et al. 2024; P. Rinaldi et al. 2025a). The nature of LRDs remains under debate. They have been interpreted as dust-reddened AGN based on the presence of broad Balmer emission lines and their red rest-frame optical colors (J. Matthee et al. 2024; D. D. Kocevski et al. 2023). However, the presence of Balmer break and some SED-fitting studies suggest that LRDs may instead be extremely compact galaxies undergoing intense starburst activity, but this leads to very high stellar mass estimates ($\sim 10^{10} M_\odot$) that are incompatible with the ΛCDM cosmological model (H. B. Akins et al. 2023; P. G. Pérez-González et al. 2024; G. Barro et al. 2024; J. F. W. Baggen et al. 2024). The Balmer absorption feature suggest they are black holes embedded in dense compton-thick, dust-free gas (K. Inayoshi & R. Maiolino 2025; R. P. Naidu et al. 2025; A. de Graaff et al. 2025; V. Rusakov et al. 2025; R. Maiolino et al. 2025; V. Rusakov et al. 2025; X. Ji et al. 2025; X. Lin et al. 2025), which may also explain the Balmer break and the observed X-ray weakness of LRDs due to heavy gas absorption. At present, there is no consensus on the physical nature of LRDs, and it remains unclear whether they represent

an early phase of black hole growth or arise from other physical processes.

In this paper, we aim to decompose the host galaxy from the AGN component and investigate the properties of the host galaxies, focusing particularly on their stellar mass and the relationship with the black hole mass. This will allow us to examine whether the M_*–$M_{\rm BH}$ relation co-evolves across cosmic time. In Section 2, we introduce our dataset and our sample. In Section 3, we describe the methods used for the image decomposition. In Section 4 we present the decomposition results. We discuss the implications in Section 5 and summarize our findings in Section 6. Uncertainties associated with the decomposition and tests of the robustness of host-flux recovery are presented in the Appendix.

Throughout this work, we use the AB magnitude system (J. B. Oke & J. E. Gunn 1983) and assume a flat ΛCDM cosmology with $\Omega_m = 0.3$, $H_0 = 70$ km s^{-1} Mpc^{-1}.

2. DATA AND SAMPLE SELECTION

The Imaging data used in this work are obtained by the JWST Advanced Deep Extragalactic Survey (JADES, A. J. Bunker et al. 2020; F. D'Eugenio et al. 2025a; E. Curtis-Lake et al. 2025; J. Scholtz et al. 2025; R. Hausen & B. E. Robertson 2022; B. D. Johnson et al. submitted; B. E. Robertson et al. submitted; C. Carreira et al. submitted). Data used in this work are released as part of the JADES DR5 data release (B. E. Robertson et al. submitted; B. D. Johnson et al. submitted). We utilize NIRCam imaging in seven wide-band filters (F090W, F115W, F150W, F200W, F277W, F356W, F444W). The native pixel scale of the NIRCam short-wavelength (SW) channel is 0.031″ per pixel, while the long-wavelength (LW) channel has a native scale of 0.063″ per pixel. All science mosaics analyzed here have been drizzled to a common pixel scale of 0.03″ per pixel to facilitate multi-band alignment and consistent photometric and morphological measurements.

J. Zhang et al. (2025) searched for broad Hα emitters in the GOODS-N field using JWST/NIRCam slitless spectroscopy from FRESCO ("First Reionization Epoch Spectroscopically Complete Observations", PID: 1895, PI: P. Oesch, P. A. Oesch et al. 2023) and CONGRESS ("Complete NIRCam Grism Redshift Survey", PID: 3577, PI: E. Egami; F. Sun et al., in prep). J. Zhang et al. (2025) identified 19 broad Hα emitters at z $\sim$ 4 - 5.5 with FWHM $>$ 1000 km s^{-1} and interpreted them as Type-I AGN galaxies; they also measured the black hole mass of these AGN galaxies based on the luminosity and FWHM of Hα broad component. All of the 19 AGN galaxies are powered by relatively low-mass black holes with masses ranging from $10^{6.65}-10^{8.29}$ $M_\odot$, which is about two orders of magnitude lower than typical quasars (X. Fan et al. 2023), while comparable to faint AGNs reported by recent JWST surveys (J. Matthee et al. 2024; J. E. Greene et al. 2024; R. Maiolino et al. 2024). Although the JADES dataset covers both the GOODS-N and GOODS-S fields, we restrict our AGN galaxy sample to the GOODS-N field because of the wider wavelength coverage of the Wide Field Slitless Spectroscopy enabled by combining CONGRESS and FRESCO. Identification of AGN galaxies in the GOODS-S field will be conducted from the ongoing GTO NIRCam Grism program PID-4549 (PI: G. Rieke).

All 19 broad Type-I AGN galaxies lie within the JADES footprint. Among them, GN1034620 overlaps with the edge of a foreground galaxy, and GN9994014 shows artificial stripping in its images. We therefore exclude these two targets from our analysis. For the remaining 17 galaxies, the image quality is sufficient for reliable image decomposition.

Among these, targets GN1089668, GN1087388, and GN1090549 have imaging available in only four bands (F090W, F115W, F356W, and F444W). Target GN1090253 has five bands available (F090W, F115W, F150W, F356W, and F444W), while GN1086855 has imaging in six bands, missing only F277W. For all other targets, imaging is available in all seven NIRCam bands. We present the false-color stamp images in Figure 1.

We take these 17 broad Type-I AGN galaxies as our final sample and use the JADES NIRCam images to perform spatial AGN–host decomposition. We describe the decomposition procedure in detail in the following section.

3. AGN-HOST IMAGE DECOMPOSITION

We first perform AGN–host image decomposition using GALFIT (C. Y. Peng et al. 2002, 2010). For each target, we extract a 50 × 50 pixel cutout (1.5″ × 1.5″) centered on the source. Although high-redshift galaxies are often characterized by irregular stellar mass and light distributions (M. Huertas-Company et al. 2024) and may exhibit multiple star-forming clumps (S. Fujimoto et al. 2024), our targets appear compact and show no obvious substructures in their images. They are only marginally resolved in the short-wavelength (SW) bands. We therefore model the AGN component using a point spread function (PSF) for each band and represent the host galaxy with a single Sérsic profile convolved with the same PSF, a common approach in AGN–host decomposition studies (X. Ding et al. 2023; Y. Harikane et al. 2023; M.-Y. Zhuang et al. 2024; C.-H. Chen et al. 2024). Our primary goal is not to resolve the internal

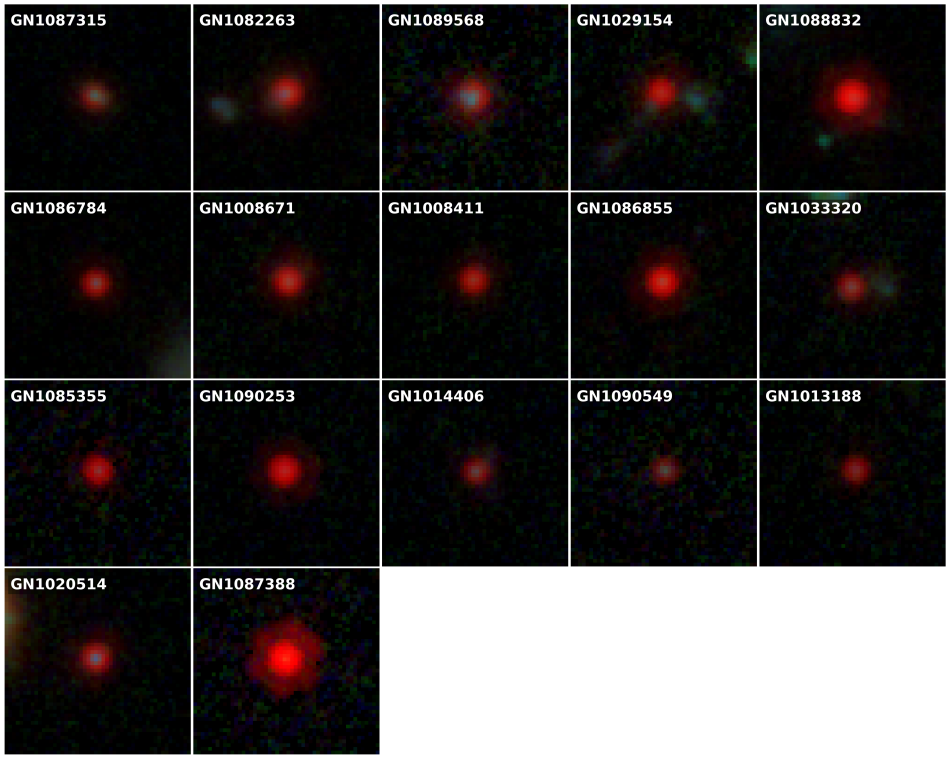

Figure 1. False-color postage ($1.5'' \times 1.5''$) stamps of the AGN-hosting galaxy sample from JWST/NIRCam cutouts. The RGB images are constructed by combining F090W+F115W (blue), F150W+F200W (green), and F277W+F356W+F444W (red). For GN1089568, GN1085355, GN1090549, and GN1087388, F090W, F115W, and the average of F356W and F444W are used for the blue, green, and red channels, respectively.

structures of the host galaxies, but rather to obtain an overall characterization of their global properties – particularly their stellar masses.

The PSF models used are mosaic PSFs generated by the JADES Team (B. E. Robertson et al. submitted), derived by injecting model PSFs calculated using STPSF (M. D. Perrin et al. 2014) into individual exposures, which are subsequently stitched together through the mosaicking procedure. These models account for both observational effects (e.g., source position on the detector, optical path differences) and data reduction processes (e.g., mosaicking). We have tested that using a different PSF does not change our conclusions significantly. For example, in a worst case scenario, even using the PSF generated for GOODS-S in Z. Ji et al. (2024) (not designed for GOODS-N pointings) introduces a bias of $\lesssim 0.3$ dex in the inferred stellar masses for our GOODS-N sample.

We first fit the F444W cutout image using only a PSF model and use the resulting center coordinates as the AGN center across all bands. Then we fit each band separately with GALFIT using a PSF model with fixed center and a Sérsic model whose center we allow to vary. During fitting, the Sérsic index n is restricted to a range of 0.7 – 8, and the effective radius R_e is constrained to 0.1 – 8 pixels ($0.003''$– $0.24''$, corresponding to ~ 0.02 – 1.46 kpc at $z = 5$). We allow the axis ratio to vary between 0.1 – 1. These parameter ranges are consistent with previous fits in the literature, e.g., M.-Y. Zhuang et al. (2024).

We selected the model from one of the SW bands to serve as the representative model for the host galaxy. This selection is based on both visual inspection and comparing reduced χ^2. The parameters from this GALFIT-derived best-fit model are adopted and convolved with PSFs to generate Sérsic models in each band.

We then use these Sérsic models, along with the point source models (PSFs), as inputs to run MCMC (Markov Chain Monte Carlo) fitting across all bands independently to determine the flux contribution from each component. We use the affine-invariant ensemble MCMC sampler implemented in emcee, keeping the PSF-based AGN model and the PSF-convolved Sérsic model fixed and allowing the MCMC to determine only their scaling coefficients and a constant background term. This yields the amount of light contributed by the point source and the Sérsic component in each band. AGN fluxes are derived accordingly, and AGN contributions are sub-

Table 1. Decomposition results of AGN galaxies

JADES ID	$z_{\rm spec}$	ΔBIC	Flag	Filter	R_e		n	Center Offset	
					(″)	(kpc)		(″)	(kpc)
(1)	(2)	(3)	(4)	(5)	(6)	(7)	(8)	(9)	(10)
GN1087315	3.91	-9661.62	Y	F150W	0.063±0.003	0.44±0.02	1.20±0.19	0.030	0.21
GN1082263	3.98	-16188.54	Y	F150W	0.058±0.004	0.40±0.03	2.60±0.38	0.034	0.24
GN1089568	4.05	-6471.49	Y	F090W	0.045±0.001	0.31±0.01	0.81±0.08	0.032	0.22
GN1029154	4.17	-256.60	X	F115W	0.124±0.230	0.85±1.57	4.90±6.60	0.016	0.11
GN1088832	4.36	-11240.28	Y	F115W	0.101±0.017	0.68±0.11	4.35±0.68	0.030	0.20
GN1086784	4.40	-186.15	X	F200W	0.060±0.038	0.40±0.26	8.00±7.15	0.009	0.06
GN1008411	4.41	-1719.09	Y	F115W	0.089±0.008	0.60±0.05	0.70±0.17	0.060	0.40
GN1086855	4.41	-177.00	X	F150W	0.240±0.733	1.60±4.89	8.00±13.90	0.018	0.12
GN1008671	4.41	-1680.73	Y	F150W	0.037±0.008	0.24±0.06	4.60±1.87	0.007	0.04
GN1033320	4.48	-749.64	Y	F115W	0.131±0.031	0.87±0.20	1.73±0.48	0.017	0.11
GN1085355	4.88	20.48	N	F115W	-	-	-	-	-
GN1090253	5.09	-1091.23	Y	F150W	0.033±0.022	0.21±0.14	4.27±4.65	0.004	0.03
GN1014406	5.15	-1030.57	Y	F115W	0.123±0.015	0.76±0.09	0.70±0.22	0.055	0.34
GN1090549	5.20	-87.18	X	F090W	0.057±0.015	0.35±0.09	0.70±0.88	0.002	0.01
GN1013188	5.25	34.04	N	F150W	-	-	-	-	-
GN1020514	5.36	-431.34	X	F115W	0.016±0.003	0.10±0.02	1.08±0.70	0.006	0.04
GN1087388	5.54	-486.64	X	F090W	0.111±0.050	0.66±0.30	1.79±1.13	0.021	0.12

NOTE— Columns: (1) IDs are from JADES DR2 F. D'Eugenio et al. (2025a). (2) Spectroscopic redshifts from J. Zhang et al. (2025). (3) BIC difference between fits using a Sérsic+PS model and a PS-only model, $\Delta\mathrm{BIC} = \mathrm{BIC}_{(\mathrm{PS+Sersic})} - \mathrm{BIC}_{(\mathrm{PS})}$. (4) Flag indicating the significance of the host-galaxy detection based on ΔBIC: "Y" for targets with confident detectable extended emission ($\Delta\mathrm{BIC} < -500$), "X" for $-500 < \Delta\mathrm{BIC} < 0$, and "N" for $\Delta\mathrm{BIC} > 0$. (5) Filter of the band image used to determine the Sérsic profile. (6) Effective radius R_e in arcsec with 1 σ uncertainties. Errors reported here are statistical errors from GALFIT and do not account for systematic effects. (7) Effective radius R_e in kpc with 1 σ uncertainties. (8) Sérsic index n with 1 σ uncertainties. (9) Offset between the centers of the PS and Sérsic components in arcsec. (10) Offset between the centers of the PS and Sérsic components in kpc.

tracted from the original images to isolate extended emission[15].

Fluxes of the extended emission are measured via aperture photometry on the AGN-subtracted images, while total fluxes are measured on the original images using the same aperture sizes. We use a circular aperture with a radius of 0.45″ and a sky annulus with inner and outer radii of 0.60″ and 0.75″, respectively. For targets with nearby sources that are blended with the target, these sources are modeled with additional Sérsic components using the same constraints described above. In such cases, aperture photometry would include contaminating flux from nearby sources; therefore, we take the flux of the Sérsic component associated with the target galaxy as the extended-emission flux. An aperture correction list is constructed for each band based on its corresponding PSF. For values of aperture correction, see J. Trussler et al. (in preparation).

Note that the Sérsic model used to describe the extended emission during MCMC fitting is assumed to have the same Sérsic parameters across all bands. The Sérsic index and effective radius of galaxies are known to vary with wavelength (B. Vulcani et al. 2014; R. Kennedy et al. 2015), although a recent study shows no significant differences between the stellar continuum sizes at different wavelengths from UV to optical (A. L. Danhaive et al. 2025). Some fitting packages, such as GALFITM and GALIGHT, attempt to account for the wavelength dependence of Sérsic parameters by performing simultaneous multi-band fitting and linking

[15] In this work, we use "extended emission" to refer to any flux not subtracted by the PSF. This emission could therefore originate from the potential host galaxy.

these parameters across bands using polynomials. However, these approaches also have limitations. The Sérsic parameters are hard to recover at LW because 1. The image resolution is worse and FWHM is broader at LW and 2. based on our fitting results, the AGN dominates at LW and such a high AGN/host flux ratio makes the estimates of Sérsic parameters deviate from the real case, as we tested in Appendix A.3.

When applying GALFITM following the setup described in M.-Y. Zhuang et al. (2024), we find that for some sources the fits in the F356W and F444W bands converge to unphysical solutions, characterized by extremely small effective radii ($\sim$ 10% of the PSF FWHM) and very large Sérsic indices that reach the imposed parameter boundaries. This behavior indicates that the GALFITM fits are unstable in these bands. In such cases, the inferred flux contribution of the Sérsic component at F444W can increase by more than 100% compared to the results obtained when fixing the Sérsic parameters from an SW band. For sources where GALFITM does not break down at long wavelengths—i.e., where it yields physically reasonable Sérsic profiles across all bands — we find consistent results between the two approaches. For example, in the case of GN1014406, GALFITM yields a stellar mass estimate of $\log(M_*) = 7.68^{+0.12}_{-0.09}$, which is consistent with the result obtained using GALFIT + MCMC ($\log(M_*) = 7.64^{+0.20}_{-0.23}$. Therefore we first use GALFIT to extract the structural information of the extended emission from a SW band, taking advantage of its higher spatial resolution, narrower PSF, and lower AGN contribution compared to the LW bands, and then fix this Sérsic profile across all bands and use MCMC fitting to decompose the flux contributions of the point source and extended components.

We also applied our method to the faint AGN-hosting galaxy GN53757 reported in I. Juodžbalis et al. (2025a), deriving a stellar mass of $\log(M/M_\odot) = 8.83^{+0.19}-0.10$. For the same source, I. Juodžbalis et al. (2025a) estimated a stellar mass of $\log(M/M_\odot) = 8.81^{+0.26}_{-0.26}$ using Forcepho (J. O. Baldwin et al. 2024).The agreement between these independent measurements demonstrates that different imaging fitting approaches yield consistent results, supporting the reliability of our method.

To determine whether extended emission is detected for each target, we also perform image fitting using a single point source (PS) model. We then evaluate whether adding the additional Sérsic component significantly improves the fit compared to using the PS model alone. The relative goodness of each fit is quantified using the Bayesian Information Criterion (BIC)

$$BIC = \chi^2 + k \ln n, \tag{1}$$

where k is the number of free model parameters, and n is the total number of data points used in the fit. For this work, our fitting has 3 free parameters (flux of Sérsic model, AGN model and background) when applying a composite Sérsic + PS model and 2 free parameters (flux of AGN model and background) when a PS-only model is applied. χ^2 measures the residual error of the model. Lower BIC values indicate a preferred balance between fit quality and model simplicity.

4. RESULTS

4.1. *Decomposition Result*

Figure 2 presents the fitting results for GN1014406 as an example. We observe extended emission left in the AGN-subtracted images in SW bands, where we believe the host galaxy has not yet been outshone by the AGN. This suggests that the emission cannot be fully explained by a point source alone. The PS+Sérsic model also gives a significantly lower BIC than the single PS model, providing strong statistical evidence for the presence of extended emission in GN1014406. The full set of fitting results for all targets is available as a figure set.[16]

In Table 1, we list the BIC difference between the PS-only model and the composite PS + Sérsic model for each target. We also report the Sérsic index and half-light radius of the best-fit Sérsic model we adopted for each target.

Among the 17 targets, 15 show lower BIC values when fitted with a composite PS + Sérsic model compared to a PS-only model, indicating that the composite model provides a better description of their surface brightness profiles and that extended emission is detected. 9 of these have $\Delta\mathrm{BIC} < -500$, which we interpret as strong detections of extended emission; this is also visually evident in the residual images of the PS-only fits. There are 6 targets which have $-500 < \Delta\mathrm{BIC} < 0$, where the BIC favors the composite model, but the residual images do not provide clear visual confirmation of extended emission. For the remaining two targets, the PS-only model yields a lower BIC, implying that their light distributions can be sufficiently described by a single point source.

When fitting our targets with a PSF and a Sérsic component, we did not enforce a common centroid for the two models. Nevertheless, we find that the spatial offset between the PSF and Sérsic centers is small, with a typical value of $\sim$ 0.12 kpc. Given this small offset, the extended emission is more likely associated with the

[16] The figures are also available here.

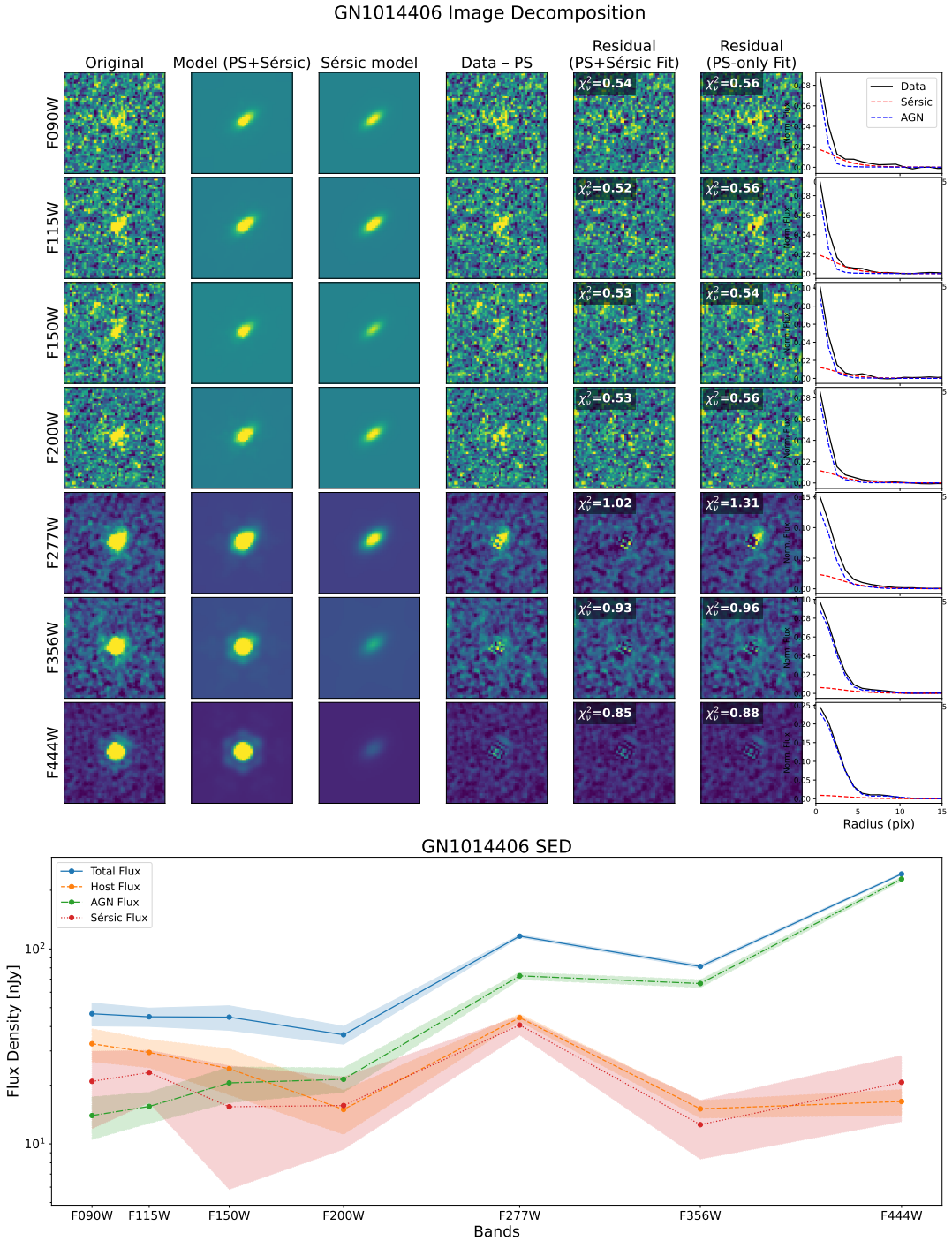

Figure 2. Top panel: AGN-Host Decompostion of GN1014406. Cutout size is $1.5'' \times 1.5''$. First column displays the orginal image in each band. Second column is the two component model (PSF + Sérsic). Third column shows the Sérsic model in each band. Fourth column show the AGN-subtracted image, where in SW bands we can find some extended emission left as a signal of host detection. Fifth column is the residue image after subtracting both PSF model and Sérsic model, with reduced χ^2 attached to each image. Sixth column shows the residue image when we attempt to fit the original image with one single PSF model, with reduced χ^2 attached. The last column displays the radial brightness profile of original data (black), Sérsic model (red), AGN model (blue). **Bottom panel:** SED of GN1014406. The blue solid curve shows the total flux. The orange dashed curve shows the host flux measured from the AGN-subtracted image. The green dash–dotted and red dotted curves show the flux of point-source and Sérsic models, respectively. The shaded regions indicate the 1σ uncertainties. The full set of fitting results for all targets is available as a figure set.

host galaxy than with spatially offset nebular emission. See Section 5.1 for detailed discussion.

We present the multi-band SED of GN1014406 in Fig. 2 as an example. The flux associated with the ex-

tended emission remains flat in f_ν across the NIRCam bands, although individual bands may be modestly enhanced by emission lines. The point-source component shows a nearly flat SED in the rest-frame UV and a red slope at LW in the rest-frame optical. In the LW bands, the total flux is dominated by the point-source contribution. The complete set of SEDs for all targets is provided in the online figure set.

In Table 2, we list the measured fluxes of the point-source and extended-emission components, together with their 1σ uncertainties. For GN1033320 and GN1029154, nearby sources blend with the target galaxy. Spectroscopic observations from CONGRESS and FRESCO confirm that these objects are foreground interlopers. To avoid contamination in the extended-emission fluxes, we take the Sérsic-model flux associated with the target galaxy instead of aperture-photometry measurements. For GN1087388 we take the Sérsic model flux for the extended emission because the AGN-subtracted image contains negative pixels, which would produce a negative aperture-photometry measurement if used directly.

4.2. *AGN-Host Spectral Energy Distributions*

Using our best-fit model obtained from GALFIT, we determine the AGN flux contribution by running MCMC. To estimate the host galaxy flux, we apply aperture photometry to the AGN-subtracted image.

We then plot the spectral energy distribution (SED) of all targets. For our targets we find that for the shorter wavelengths the flux can be dominated either by the extended emission or by the point source. However, we find that for F356W and F444W, over ∼50% and over ∼70% of light comes from point source in F356W and F444W.

We conducted SED fitting with PROSPECTOR (B. D. Johnson et al. 2021) combined with the Parrot artificial neural network (ANN) emulator for acceleration (E. P. Mathews et al. 2023), following Y. Zhu et al. (2024). Source redshifts $z_{\rm spec}$ have been fixed from the center location of the Hα narrow component.

J. Zhang et al. (2025) also performed SED fitting for these targets based on (NIRCam + HST) photometry alone but without image decomposition. Their SED fitting was also performed with PROSPECTOR, but with updated empirical models of the AGN torus emission and hot dust emission from the host galaxy (see J. Lyu et al. 2024 for details). We compare our SED fitting results based on image decomposition with their results. In our SED fits, which use the decomposed images, we find that the LW fluxes are dominated by the point source, which we interpret as being due to the AGN. In contrast, J. Zhang et al. (2025) find that only half of the sources show MIRI AGN evidence from SED fitting. We present the comparison for some targets in Figure 3. The full set of SED fitting results for all targets is available as a figure set.[17]

We find that our SEDs of extended emission resemble the host components' underlying stellar populations in J. Zhang et al. (2025)'s fitting when AGN evidence is prominent. When the decomposed SEDs show no AGN evidence, the J. Zhang et al. (2025)'s fits attribute most of the flux to the host's stellar component and exceed by much our estimates of the hosts' emission.

5. DISCUSSION

5.1. *The nature of the extended emission*

Our sample is selected as broad Hα emitters with $\mathrm{FWHM_{H\alpha,\ broad}} > 1000$ km/s (J. Zhang et al. 2025). Such a broad component strongly indicates the existence of an AGN. Based on this assumption, we performed the image decomposition using a PS model to represent the AGN and a Sérsic model to describe any extended emission.

When we perform the image decomposition, we find residual flux detected for 9 out of 17 targets in our sample. There could be several interpretations for the residual signal after subtracting the AGN model. One possibility is that this is the host galaxy (P. Rinaldi et al. 2025a). This is physically reasonable as when we fit targets with one PSF and one Sérsic model, the offset between the AGN and Sérsic centroids is less than 0.06" ($\lesssim 0.36$ kpc). Study of local LRD analogs suggests extended features clearly visible at lower redshift ($z \sim 2$) would be hard to detected if observed at $z \sim 7$ due to cosmological surface brightness dimming (P. Rinaldi et al. 2025b). The fraction of targets in which we detect extended emission ($\sim 53\%$) is consistent with the fraction of LRDs reported to host extended components in previous studies ($\sim 50\%$, P. Rinaldi et al. 2025a). Another possibility is that the residual signal arises from nebular emission (C.-H. Chen et al. 2024). In some LRDs, extended emission has been found to be spatially offset from the AGN component, and in several cases the extended emission is better fit by a pure nebular-emission model (C.-H. Chen et al. 2025). I. Labbe et al. (2025) also proposed that the blue rest-frame UV (ultraviolet) light could arise from scattered AGN emission. However, the non-detection of He II λ1640 and Mg II $\lambda\lambda$2796, 2803 together with the high equivalent

[17] The figures are also available here.

Table 2. Photometry from Imaging decomposition.

JADES ID	Component	F090W [nJy]	F115W [nJy]	F150W [nJy]	F200W [nJy]	F277W [nJy]	F356W [nJy]	F444W [nJy]
GN1087315	Extended Emission	45.1±3.6	35.5±3.2	43.2±3.2	53.6±3.7	64.0±0.9	53.9±1.0	25.9±1.1
	Point Source	18.3±2.7	18.5±2.4	22.2±2.7	29.7±4.0	83.4±2.3	163.6±3.1	107.0±3.7
GN1082263	Extended Emission	76.0±2.5	76.7±3.2	69.5±4.1	90.1±2.6	112.1±1.5	88.4±1.2	56.0±1.4
	Point Source	17.6±2.0	18.9±2.4	21.2±3.5	44.5±3.1	205.6±4.5	377.5±4.4	422.1±5.1
GN1089568	Extended Emission	170.6±7.2	181.7±6.0	-	-	-	142.2±2.9	82.8±5.9
	Point Source	35.3±6.3	39.3±5.3	-	-	-	356.3±11.0	314.9±22.2
GN1029154	Extended Emission	13.8±3.3	11.1±2.6	6.4±4.0	8.3±4.7	32.4±3.9	45.6±3.7	42.0±6.2
	Point Source	3.3±1.5	4.2±1.2	9.1±2.1	19.6±2.6	111.7±2.4	333.1±2.5	394.8±4.1
GN1088832	Extended Emission	43.0±3.6	46.8±2.1	45.3±3.0	52.1±3.9	-	105.7±0.9	102.7±1.2
	Point Source	4.0±2.6	11.2±1.6	15.3±2.5	22.8±4.4	-	250.0±3.1	1161.5±5.0
GN1086784	Extended Emission	7.3±2.3	8.9±3.3	4.5±3.9	10.7±2.6	18.9±1.2	13.3±1.4	18.1±1.3
	Point Source	15.3±2.9	19.6±4.3	20.2±6.1	25.0±5.1	107.7±5.3	281.4±7.7	185.7±7.8
GN1086855	Extended Emission	24.2±2.7	0.6±4.0	21.1±6.1	10.0±3.0	-	64.9±2.8	5.7±2.1
	Point Source	19.5±2.4	21.3±3.7	28.6±6.0	45.5±3.8	-	515.3±10.0	439.0±4.0
GN1008671	Extended Emission	42.7±4.4	50.8±3.3	52.4±5.5	76.6±4.6	117.9±1.9	94.2±1.6	118.8±2.5
	Point Source	0.6±2.3	0.5±1.8	2.5±6.4	5.0±9.3	115.1±11.5	365.1±12.4	291.3±21.3
GN1008411	Extended Emission	8.6±5.2	6.6±2.3	18.8±3.4	16.3±6.3	32.8±1.9	26.3±0.9	30.6±1.0
	Point Source	6.1±3.3	7.6±1.3	11.1±2.1	20.3±5.3	95.7±3.4	231.0±2.1	270.0±2.2
GN1033320	Extended Emission	23.0±4.1	32.4±2.9	23.3±4.2	29.5±2.9	42.0±2.6	38.5±2.6	16.9±4.0
	Point Source	14.2±1.4	12.5±1.0	16.5±1.6	23.6±1.2	99.3±1.6	194.1±1.7	168.5±2.6
GN1090253	Extended Emission	38.2±7.2	18.3±2.3	12.5±3.6	-	-	83.4±1.1	62.6±1.2
	Point Source	1.9±5.6	4.7±3.6	5.5±6.4	-	-	202.7±8.2	432.2±10.1
GN1014406	Extended Emission	32.6±6.2	29.5±4.8	24.3±6.4	15.0±3.8	44.4±1.9	15.1±1.6	16.5±2.5
	Point Source	14.0±3.4	15.6±2.8	20.6±4.3	21.5±3.1	72.8±3.1	66.5±3.0	228.5±5.5
GN1090549	Extended Emission	23.1±6.9	31.7±5.7	-	-	-	37.9±2.6	1.5±5.8
	Point Source	8.1±6.0	12.4±5.1	-	-	-	41.7±12.1	146.0±18.5
GN1020514	Extended Emission	87.1±5.0	49.3±4.0	40.3±6.4	68.8±4.0	72.1±2.3	18.3±1.8	55.1±2.7
	Point Source	26.7±17.3	36.3±12.1	34.3±21.9	35.4±18.7	161.6±32.6	334.7±15.3	399.0±52.1
GN1087388	Extended Emission	28.1±15.5	25.8±13.2	-	-	-	79.4±14.7	118.6±25.8
	Point Source	16.6±5.5	45.6±5.2	-	-	-	841.2±11.7	2156.7±22.6

widths (EW) of C III] and C IV makes this interpretation less likely (H. B. Akins et al. 2025).

With the current imaging data, it is difficult to uniquely distinguish whether it originates from a stellar component or nebular emission. Follow-up deep JWST/NIRSpec IFU observations would help determine the true nature of the residuals by separating the stellar continuum from the nebular line emission, e.g.,M. A. Marshall et al. (2025).

An important caveat applies to two targets in our sample (GN1033320, GN1029154) where the residual light initially appeared to be due to companion galaxies. After examining their spectra, we found that: 1. both objects are actually foreground interlopers; 2. their morphologies resemble off-centered nebular emission; and 3. without spectroscopic confirmation, they can be easily misinterpreted as companions or nebular emission. This highlights that imaging alone can be misleading. Nebular emission and foreground galaxies can mimic host features.

For the extended emission observed in faint AGN-hosting galaxies, C.-H. Chen et al. (2024) suggest that it may arise from nebular emission rather than a stellar component, based on the presence of an offset between the AGN position and the centroid of the extended emission. However, for some sources, pure nebular-emission

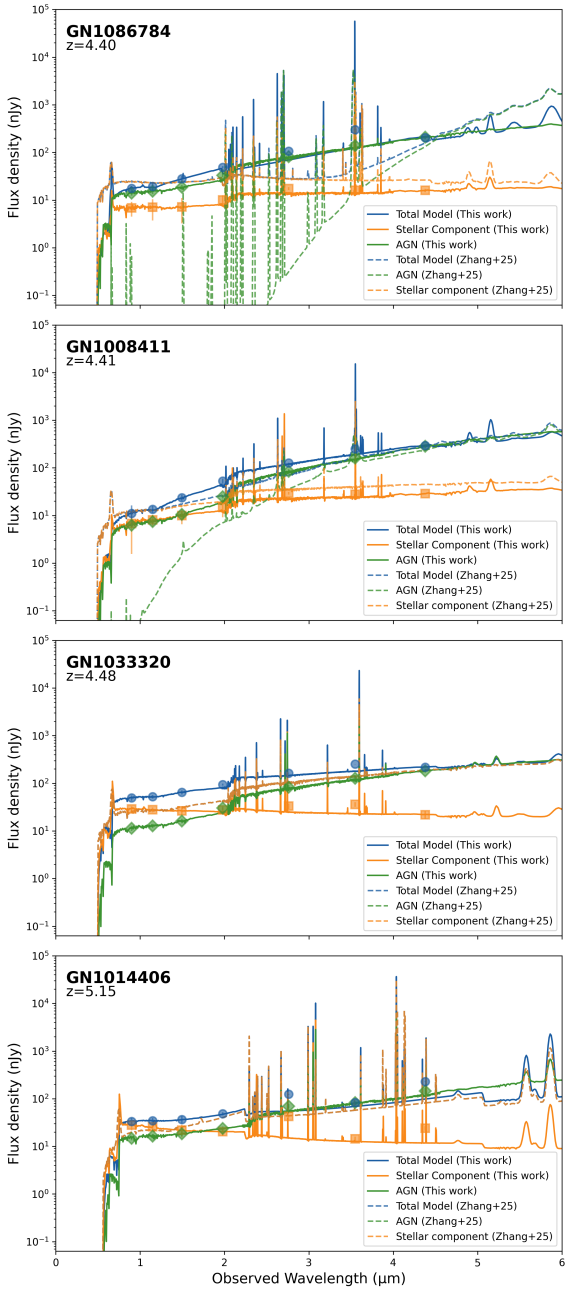

Figure 3. SED fits for four selected targets. Green curves show the AGN component, orange curves the stellar component, and blue curves the total model flux. Solid lines correspond to results based on image decomposition. Model-predicted fluxes are shown as symbols: blue circles for the total flux, orange squares for the stellar component, and green diamonds for the AGN component. Dashed lines indicate photometry-based SED fitting performed without image decomposition. The top two panels present cases in which AGN signatures are clearly detected in the photometry-based SED fits, while the bottom two panels show sources for which the photometry-based SED fitting alone does not clearly identify an AGN component. The full set of SED fitting results for all targets is available as a figure set.

models fail to reproduce the observed fluxes (C.-H. Chen et al. 2025). In our sample, we find no obvious offset between the centroid of the point source (i.e., the AGN) and that of the extended emission. In addition, the inferred half-light radii and stellar masses are consistent with empirical size–mass relations. We therefore interpret the extended component as the host galaxy and examine its properties under this assumption. Host-galaxy properties, including stellar mass, are derived from SED fitting.

Finally, a caveat of our analysis is that, although we have attempted to separate the AGN and host flux through PS+Sérsic decomposition, we cannot rule out the possibility that some fraction of the host mass is highly concentrated in the central region and therefore mimics point-like emission, even at the JWST/NIRCam spatial resolution. As tested in Appendix A, compact Sérsic radial-profile can be recovered as long as they are not extremely compact relative to the PSF. If such an unresolved central component exists, and if we trust the SED-based stellar mass estimates, then these host galaxies would have an extremely concentrated mass distribution, while still showing some extended emission in the SW bands. In either case, whether the high $M_{\rm BH}/M_*$ ratios revealed by our image decomposition (and by previous work) are real, or the host galaxies are so compact that part of their mass cannot be separated from the AGN, the results support an inside-growth picture for these AGN-host systems.

5.2. *Host-Galaxy Properties*

We list the stellar masses for all targets with detected hosts in Table 3, along with the black hole and stellar masses reported by J. Zhang et al. (2025). We then compare our stellar-mass measurements with those reported in J. Zhang et al. (2025), with four examples shown in Fig. 4. The complete set of SED fitting results and comparisons with J. Zhang et al. (2025) is available on GitHub.

For targets in which an AGN component is identified in SED fitting of J. Zhang et al. (2025), the SED of the host galaxy derived from our image decomposition closely resembles the stellar component SED in their results. Consequently, we find consistent stellar mass estimates, with differences typically $\lesssim 0.5$ dex. In contrast, for targets without evidence for an AGN component in their photometry-based SED fitting, the inferred host-galaxy SED from our analysis differs significantly from theirs, leading to substantially different stellar mass estimates. In these cases, our stellar masses are ~ 0.9–1.8 dex lower than those reported in J. Zhang et al. (2025).

Table 3. Black hole mass and stellar mass of the AGN galaxies with host detection

JADES ID	$\log(M_{\rm BH}/M_\odot)$	$\log(M_{*,\,\rm decom.}/M_\odot)$	$\log(M_{*,\,\rm SED}/M_\odot)$	AGN Evidence
(1)	(2)	(3)	(4)	(5)
GN1087315	7.01 ± 0.11	$7.89^{+0.10}_{-0.11}$	8.76 ± 0.28	N
GN1082263	6.65 ± 0.17	$8.58^{+0.08}_{-0.15}$	8.77 ± 0.40	Y
GN1089568	7.04 ± 0.09	$8.91^{+0.07}_{-0.24}$	8.76 ± 0.25	Y
GN1029154	7.38 ± 0.10	$8.65^{+0.17}_{-0.42}$	8.12 ± 0.32	Y
GN1088832	7.85 ± 0.04	$9.22^{+0.11}_{-0.25}$	9.64 ± 0.21	Y
GN1086784	7.71 ± 0.15	$8.27^{+0.16}_{-0.22}$	8.38 ± 0.29	Y
GN1086855	7.28 ± 0.14	$8.32^{+0.01}_{-0.01}$	8.85 ± 0.43	Y
GN1008671	7.59 ± 0.04	$8.78^{+0.16}_{-0.05}$	10.14 ± 0.46	N
GN1008411	7.72 ± 0.21	$8.41^{+0.20}_{-0.52}$	8.66 ± 0.64	Y
GN1033320	7.22 ± 0.19	$8.81^{+0.07}_{-0.07}$	9.76 ± 0.38	N
GN1090253	7.13 ± 0.07	$9.17^{+0.01}_{-0.01}$	9.31 ± 0.50	Y
GN1014406	7.81 ± 0.18	$7.64^{+0.20}_{-0.23}$	9.30 ± 0.42	N
GN1090549	7.19 ± 0.16	$8.73^{+0.08}_{-0.10}$	9.09 ± 0.19	Y
GN1020514	7.22 ± 0.08	$8.32^{+0.08}_{-0.08}$	10.14 ± 0.42	N
GN1087388	8.29 ± 0.02	$9.90^{+0.23}_{-0.45}$	10.87 ± 0.26	N

NOTE—Columns: (1) ID of the AGN. (2) Black Hole masses reported by J. Zhang et al. (2025). (3) Stellar mass estimates derived from SED fitting based on imaging decomposition results. (4) Stellar mass estimates reported by J. Zhang et al. (2025), from photometry-based SED fitting. (5) Whether AGN evidence is prominent in photometry-based SED fitting (J. Zhang et al. 2025).

These discrepancies arise from differences in how flux is attributed between the stellar and AGN components. SED fitting based solely on photometry may be unable to robustly separate multiple components. In cases where the SED fit correctly identifies a non-negligible AGN component, the inferred stellar masses are broadly consistent with those obtained when the host and AGN are separated via image decomposition. However, when the AGN contribution is not recognized (or is weak enough to be absorbed by other SED degrees of freedom), a substantial fraction of the flux can be incorrectly assigned to the stellar component,leading to an overestimation of the stellar mass by ∼1–2 dex. Another reason that SED fitting from J. Zhang et al. (2025) gives a higher stellar mass estimate is it relies on HST + NIRCam data alone for fitting while longer wavelength data is not available. Including MIRI and ALMA data can lead to a ~ 0.6 dex decrease in stellar mass estimation compared to fits based only on HST + NIRCam data even assuming pure stellar origin(C. C. Williams et al. 2024; T. Wang et al. 2025).

Similar conclusions were reached by P. G. Pérez-González et al. (2024), who estimated stellar masses using multiple SED modeling approaches with different assumptions about the relative contributions of stellar and AGN emission. Using the PROSPECTOR-AGN framework, in which stellar emission is constrained to dominate the rest-frame UV while AGN emission dominates from the optical to infrared, they derived typical stellar masses that are consistent to those inferred for our targets. When using PROSPECTOR-AGN+, in which the AGN contribution is allowed to vary, the derived stellar mass remains consistent with PROSPECTOR-AGN in cases with prominent AGN emission. In contrast, for sources with no significant AGN evidence, the inferred stellar mass is more than 1 dex higher. However, in the absence of imaging-based decomposition, there is no strong justification for constraining the relative contributions of the stellar and AGN components rather than allowing them to vary freely, especially when mid-infrared data are missing.

5.3. *Size-Mass Relation*

In Fig. 5, we present the stellar mass–size relation for our sample, overplotted with the size–mass relations from N. Allen et al. (2025) and A. L. Danhaive et al. (2025). For our analysis, we adopt the Sérsic model derived from a representative SW band, which can range from F090W to F200W, but is most commonly selected from F115W or F150W. To enable a consistent com-

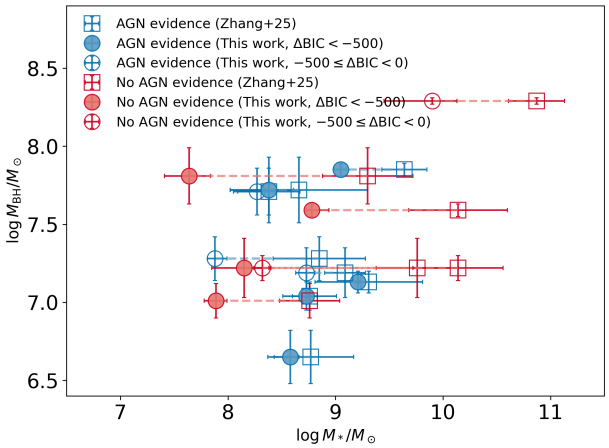

Figure 4. Comparison of stellar mass estimates. Stellar masses derived from our analysis are shown as circles, while those from J. Zhang et al. (2025) are shown as squares. Measurements for the same sources are connected by dashed lines. Targets with AGN evidence in total-photometry based SED fitting are shown in blue, while the remaining sources are shown in orange.

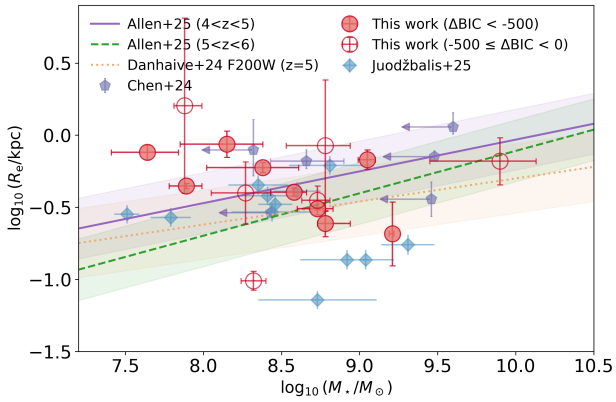

Figure 5. Stellar mass–size relation for our sample. Effective radii obtained from imaging-based AGN–host decomposition are shown as red circles for $z \sim 4$–5 targets and red squares for $z \sim 5$–6 targets. The solid line and dashed line with shaded regions represent the best-fit size–mass relations and intrinsic scatter from N. Allen et al. (2025) in the corresponding redshift bins. The dotted line shows the size–mass relation from A. L. Danhaive et al. (2025). Measurements from C.-H. Chen et al. (2024) and I. Juodžbalis et al. (2025a) are included as purple pentagons and blue diamonds for comparison.

parison, we therefore use the F150W size–mass relation from N. Allen et al. (2025) and F200W size–mass relation from A. L. Danhaive et al. (2025). The majority of our data points fall within the $\pm 1\sigma$ scatter of this relation. We also include measurements from C.-H. Chen et al. (2024), whose size–mass relation is broadly consistent with our results. Our results suggest that the extended emission is likely from the host galaxy.

5.4. $M_{BH} - M_*$ Relation

Figure 6 shows the inferred stellar and black hole masses for our targets, together with results from other studies. We compare our measurements to AGN of similar black hole masses identified in recent JWST surveys (Y. Harikane et al. 2023; R. Maiolino et al. 2024; Á. Bogdán et al. 2024), and to the local M_{BH}/M_* relation reported by A. E. Reines & M. Volonteri (2015) and J. E. Greene et al. (2020).

For objects with detected host galaxy emission, the inferred black holes appear extremely overmassive relative to their host galaxies when compared to the local relation of A. E. Reines & M. Volonteri (2015). When compared to the local relation from J. E. Greene et al. (2020), which is suggested to be more robust and less sensitive to galaxy type (Y. Sun et al. 2025), the inferred M_{BH}/M_* ratios lie closer to the local relation.

The stellar masses derived for our targets are typically a factor of $\sim$ 100–1000 lower than expected from the local M_{BH}–M_* relation. This extreme offset suggests that black holes in these early AGN may grow more rapidly than their host galaxies, or that star formation in the host galaxies is significantly suppressed, potentially by AGN feedback. Many recently discovered faint AGN at high redshift have also been reported to lie above the local relation, hosting black holes that are overmassive relative to their stellar mass; for our sample, this discrepancy appears even more pronounced.

Our M_{BH}/M_* ratios span 0.01–1.48. This range is broadly consistent with the results based on image decomposition for LRDs (0.02–1.38; C.-H. Chen et al. 2024). For comparison, faint AGN galaxies analyzed using NIRSpec prism spectra and multiband photometry yield lower ratios of 0.002–0.22 (I. Juodžbalis et al. 2025a). The M_{BH}/M_* ratios of LRDs from B. L. Jones et al. (2025) is inferred from SED-fitting alone as well. Although they performed image decomposition using NIRCam imaging data, this decomposition was used only to assess whether extended emission is present. The total flux was still taken as the input for SED fitting, with the flux attribution between the AGN and the host galaxy determined entirely by the SED fitting.

This difference is expected. When we compare our stellar mass estimates to those obtained from purely photometry-based SED fitting, we find that the latter can be 1–2 dex higher, especially when AGN emission is not strongly evident in the SED fitting based on total photometry. In such cases, the stellar continuum may be overestimated, leading to larger inferred stellar

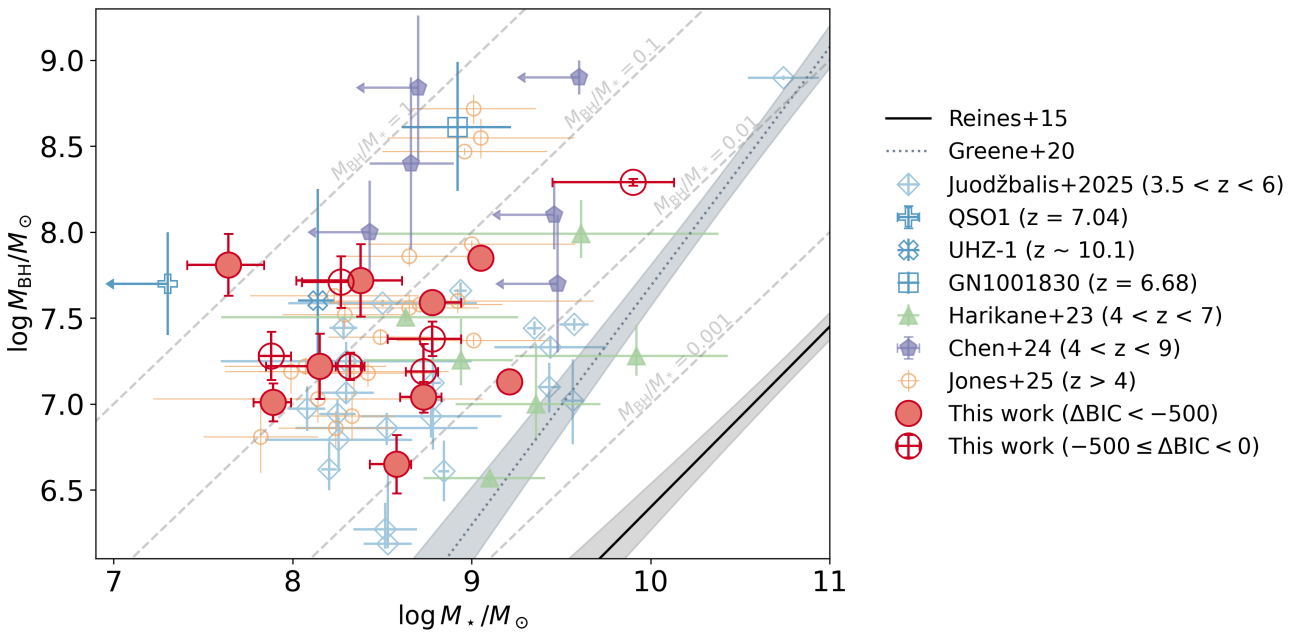

Figure 6. BH mass versus host galaxy stellar mass. Targets for which we detect emission from the host galaxy are shown as red solid circles. Green triangles are measurements from Y. Harikane et al. (2023), where they decomposed the AGN/Host galaxy for faint type-1 AGN using JWST/NIRCam and HST data. Purple pentagons show measurements of broad-line AGN from C.-H. Chen et al. (2024) based on image decomposition. Light-blue diamonds are measurements from I. Juodžbalis et al. (2025a) where stellar masses were estimated with SED fitting based on total photometry. UHZ-1, QSO1, and GN1001830 are shown as a blue cross, a plus symbol, and a square, respectively. Orange circles are stellar mass estimates of LRDs from B. L. Jones et al. (2025). The solid black and dotted gray lines are the local $M_{BH} - M_*$relation inferred by A. E. Reines & M. Volonteri (2015) and J. E. Greene et al. (2020), with uncertainties represented by the shaded regions. Green dashed lines correspond to $M_{BH}/M_* = 1$, 0.1, 0.01 and 0.001.

masses and lower M_{BH}/M_* ratios. A similar effect is also reported in I. Juodžbalis et al. (2025a), where stellar mass estimates derived from image decomposition are lower than those obtained from spectra-based SED fitting by up to ∼2.5 dex, and lower than those from SED fitting based on total photometry by up to ∼1.2 dex.

We also include AGN galaxies from Y. Harikane et al. (2023), where stellar masses are also derived using image decomposition. Their sample selection differs from ours: they did not restrict the AGN hosts to be compact, leading to systematically higher stellar masses in their sample.

Some of our sources have extreme M_{BH}/M_* ratios above 0.1. There are several sources reported in literature having extreme M_{BH}/M_* ratios as well, like UHZ1 (Á. Bogdán et al. 2024; A. D. Goulding et al. 2023), QSO1 (L. J. Furtak et al. 2025, 2024; F. D'Eugenio et al. 2025b; I. Juodžbalis et al. 2025b), GN1001830 (I. Juodžbalis et al. 2024), suggesting that it may be a common feature for supermassive black holes (SMBHs) to grow more rapidly than their host galaxies in the early universe. The high BH mass and high ratio of M_{BH}/M_* of these sources are used to support the heavy black hole seeding scenario, such as Direc Collapse Black Holes (P. Natarajan et al. 2024; I. Juodžbalis et al. 2025b). The similarly elevated M_{BH}/M_* ratios in our targets imply that the host galaxies may be suppressed or underdeveloped, possibly due to AGN feedback.

The black hole masses we used here are measured by J. Zhang et al. (2025), who used single-epoch virial estimators proposed by A. E. Reines et al. (2013),

$$\begin{aligned}\log_{10}(M_{BH}/M_\odot) = 6.57 + \log_{10}(\epsilon) + \\ 0.47\log_{10}(L_{H\alpha,broad}/10^{42}\,erg\,s^{-1}) + \\ 2.06\log_{10}(FWHM_{broad}/10^3\,km\,s^{-1}).\end{aligned} \quad (2)$$

This approach assumes the broadening of Hα is entirely due to Doppler motions. However, the applicability of single-epoch virial mass estimators at high redshift remains uncertain, as there are currently no direct calibration measurements beyond $z \gtrsim 2$. V. Rusakov et al. (2025) proposed that little red dots (LRDs) may host young supermassive black holes embedded in dense ionized gas, where emission lines are significantly broadened by electron scattering rather than

purely by virial motions. Under this scenario, the inferred black hole masses are 2 dex lower than the scenario with only Doppler broadening. Under this scenario, black hole masses inferred assuming pure Doppler broadening could be overestimated by up to ∼2 dex. If correct, this would substantially alleviate the apparent tension between the high $M_{\rm BH}/M_*$ ratios observed at high redshift and local scaling relations. Yet, a direct, dynamical black hole mass measurement for an LRD results in a value consistent with those obtained from single epoch viral relation (I. Juodžbalis et al. 2025b), suggesting that black holes in faint high-redshift galaxies may indeed be intrinsically overmassive.

6. CONCLUSION

In this study, we perform spatially resolved AGN–host galaxy decomposition for a sample of 17 broad-line AGN galaxies at $z \sim 5$ using deep JWST/NIRCam imaging from the JADES survey. Our sample consists of broad Hα emitters at $z = 3.7$–6.5 identified in the CONGRESS and FRESCO surveys. The image decomposition is carried out using JADES NIRCam observations in up to seven wide bands (F090W–F444W).

We use a two-component model consisting of a Sérsic profile to represent the host galaxy and a point source to represent the AGN. Structural parameters of the Sérsic component are determined using GALFIT, while the flux contributions of the AGN and host galaxy in each band are estimated using MCMC fitting.

Our key results are as follows:

- Among the 17 broad-line AGN galaxies in our sample, we detect extended host-galaxy emission in 9 targets. For 6 sources, the fit doesn't show a significant improvement when using a two-component (PS + Sérsic) model compared to a single PS model (-500 $<\Delta$ BIC $<$ 0). For the remaining 2 sources, PS + Sérsic model does not improve the fit relative to a single PS model. The radial profiles of these two targets in both short-wavelength (SW) and long-wavelength (LW) bands closely follow the PSF, indicating that their emission is AGN-dominated across all bands.

- We perform SED fitting using the host-galaxy fluxes derived from our image decomposition. We find that incorporating image decomposition into the SED fitting can lead to stellar mass estimates 1–2 dex lower than those obtained from SED fitting without image decomposition when the AGN component is not identified. In cases where clear AGN signatures are already present in SED fitting based on total photometry, the derived stellar masses remain consistent, typically differing by $\lesssim 0.6$ dex.

- The detected host galaxies exhibit relatively low stellar masses compared to their black hole masses, resulting in a significant offset from the local scaling relation. Elevated $\rm M_{BH}/M_*$ ratios have also been reported in other LRD surveys; however, our targets show systematically higher ratios compared to results based on photometry-only SED fitting without image decomposition. In contrast, when compared to LRDs whose stellar masses are derived using imaging-based decomposition, our inferred ratios are consistent.

We demonstrate that extended emission can be robustly identified in ∼53% of galaxies hosting faint AGN. By performing imaging-based AGN–host decomposition, we recover the host-galaxy's SED and from the latter derive its physical properties Our results highlight the importance of spatially separating AGN and host emission when characterizing the stellar content of faint AGN populations. Future work incorporating spatially resolved spectroscopic observations will allow us to directly link host-galaxy structure to AGN activity, providing deeper insight into the co-evolution of faint AGNs and their host galaxies.

ACKNOWLEDGMENTS

ZM, EE, YZ, and CNAW acknowledge support from the NIRCam Science Team contract to the University of Arizona, NAS5-02105. YZ is also supported by JWST Program #6434. Support for program #6434 was provided by NASA through a grant from the Space Telescope Science Institute, which is operated by the Association of Universities for Research in Astronomy, Inc., under NASA contract NAS 5-03127. AJB acknowledges funding from the "FirstGalaxies" Advanced Grant from the European Research Council (ERC) under the European Union's Horizon 2020 research and innovation program (Grant agreement No. 789056). SC acknowledges support by European Union's HE ERC Starting Grant No. 101040227 - WINGS. ECL acknowledges support of an STFC Webb Fellowship (ST/W001438/1). RM acknowledges support by the Science and Technology Facilities Council (STFC), by the ERC through Advanced Grant 695671 "QUENCH", and by the UKRI Frontier Research grant RISEandFALL. RM also acknowledges funding from a research professorship from the Royal Society. XJ acknowledges support by the Science and Technology Facilities Council (STFC), by the ERC through Advanced Grant 695671 "QUENCH", and

by the UKRI Frontier Research grant RISEandFALL. ST acknowledges support by the Royal Society Research Grant G125142. HÜ acknowledges funding by the European Union (ERC APEX, 101164796). Views and opinions expressed are however those of the authors only and do not necessarily reflect those of the European Union or the European Research Council Executive Agency. Neither the European Union nor the granting authority can be held responsible for them.

This work is based on observations made with the NASA/ESA/CSA James Webb Space Telescope. The data were obtained from the Mikulski Archive for Space Telescopes at the Space Telescope Science Institute, which is operated by the Association of Universities for Research in Astronomy, Inc., under NASA contract NAS 5-03127 for JWST.

The authors acknowledge the FRESCO team for developing their observing program with a zero-exclusive-access period.

All the JWST data used in this paper can be found in MAST: https://doi.org/10.17909/8tdj-8n28.

This material is based upon High Performance Computing (HPC) resources supported by the University of Arizona TRIF, UITS, and Research, Innovation, and Impact (RII) and maintained by the UArizona Research Technologies department. This project made use of lux supercomputer at UC Santa Cruz, funded by NSF MRI grant AST 1828315.

We respectfully acknowledge the University of Arizona is on the land and territories of Indigenous peoples. Today, Arizona is home to 22 federally recognized tribes, with Tucson being home to the O'odham and the Yaqui. The university strives to build sustainable relationships with sovereign Native Nations and Indigenous communities through education offerings, partnerships, and community service.

Facilities: JWST, MAST

Software: `GALFIT` (C. Y. Peng et al. 2002, 2010) `PROSPECTOR` (B. D. Johnson et al. 2021)

APPENDIX

A. TESTING THE ROBUSTNESS OF HOST GALAXY FLUX RECOVERY

Separating the emission from an AGN and its host galaxy has long been a difficult task, particularly at high redshift where quasar hosts are extremely compact and the AGN overwhelmingly dominates the observed light (X. Ding et al. 2023). Although the AGNs in our sample are relatively faint—mitigating this issue to some extent—the decomposition remains non-trivial. When GALFIT returns a very compact Sérsic component, we are especially concerned about degeneracies between this compact Sérsic model and the point source model.

Recovering the host galaxy flux in the LW bands is even more challenging. In F356W and F444W, the NIRCam images of our targets appear unresolved, and for systems with host detections, the AGN contributes more than 50% of the total light. The radial flux profiles in these bands closely resemble those of a point source, indicating that the host galaxy is strongly outshone by the AGN. In addition, the LW PSFs are intrinsically broader and less well-resolved than those in the SW channels, further increasing the degeneracy between the AGN and host components. Consequently, a fraction of the stellar emission may be misassigned to the AGN during decomposition, or conversely, AGN light may be incorrectly attributed to the host.

To assess the reliability of our host flux measurements , we performed a series of mock experiments. We selected a compact galaxy at $z = 4.83$ in GOODS-N field, GN1034159, from the JADES NIRCam and NIRSpec catalogs. We first fit this galaxy with one point source and one Sérsic model, the same as the procedure for our sample described earlier. The fit using F115W gives an estimate of Re = 0.38 kpc and n = 1.46. These values are similar to the best-fit models we derived for the host galaxies of our sample so we believe this galaxy can represent the host galaxy in our sample well. Using this galaxy as template for the host galaxies we constructed mock galaxy images to test AGN–host decomposition performance.

A.1. *The effects of AGN-host flux ratios*

We first test how the AGN/host flux ratio may affect the recovery of the host's flux. To create the mock data, we added scaled AGN model images on top of each galaxy image. Each AGN component was scaled such that the AGN-to-host flux ratio takes values in the range [0, 0.1, 0.5, 1.0, 1.5, 2.0, 2.5, 3.0, 5.0, 10.0, 20.0, 30.0, 40.0, 50.0, 60.0, 70.0, 80.0, 90.0, 100.0, 200.0, 1000.0, 10000.0, 100000.0], producing a series of synthetic AGN-contaminated galaxies.

We included Poisson noise from the AGN by adding its contribution to the error map and injecting corresponding random Gaussian noise into the science image to account for the additional noise expected when a real AGN is present.

We fit the real galaxy images with GALFIT, using a composite Sérsic + PS model. The best-fit Sérsic model from the band with the most reliable fit was then taken as the representative host model. This representative model was subsequently convolved with the PSF in each band to generate host models. Together with the PS model, these Sérsic models were used as inputs to our MCMC fitting procedure, which we applied to each mock image to determine the recovered host and AGN fluxes.

We compared the recovered host fluxes with the true host fluxes, measured through aperture photometry on the original galaxy images. The ratio of recovered to true fluxes in each band is shown in Fig. 7. Even when no AGN component is added, fitting a PS model plus a Sérsic model introduces a systematic bias—particularly in the F444W band—because the model is forced to divide the central light between the Sérsic and PS components, leading to a fraction of the host flux being misassigned to the PS model. In real galaxies, any intrinsically compact central light concentration could therefore be incorrectly interpreted as an AGN.

The recovery of host–galaxy fluxes depends strongly on the AGN/host ratio. As the AGN contribution increases, the decomposition becomes more degenerate, which causes the recovered host flux to deviate more from the true value. Also, when we inject AGN models, the Poisson noise we added grows as the flux of the AGN model we injected increases. When we add an AGN model with flux 10000 brighter than the galaxy, the noise is comparable to the host's flux.

From F090W to F200W, the difference between the injected and recovered host flux stays below 15% for AGN/host ratios up to ~ 1000. In F277W, the recovery remains accurate (within 15%) only when the AGN/host ratio is below $\sim$200. At longer wavelengths, the breakdown occurs at even lower AGN/host ratios. In F356W, reliable recovery (difference $< 15\%$) is maintained only for AGN/host ratios below 40.

F444W is more challenging. Due to the poor spatial resolution and stronger PSF–Sérsic degeneracy, even at AGN/host ratio = 0 the recovered host flux reaches only 84.4% of the true value. This intrinsic bias reflects the limited ability to distinguish a compact host from the PSF in the longest–wavelength band. This demonstrates that the ability of recovering the host flux is strongly dependent on the resolution of the filter.

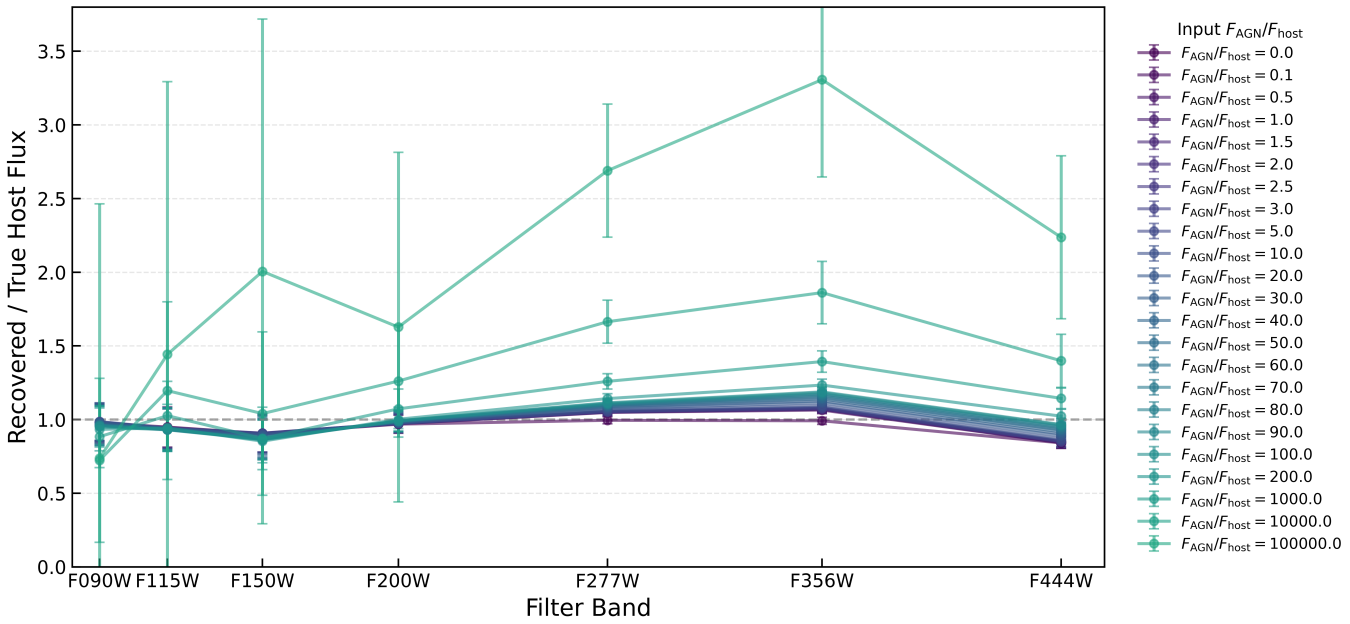

Figure 7. Ratio of recovered host fluxes to real host fluxes. Each color denotes a different injected AGN-to-host flux ratio (legend). Recovered host fluxes are consistent with the true values within $\sim$ 10 % across most bands. At higher AGN/host ratios the scatter increases, yet the decomposition remains stable even for AGN-dominated cases up to a ratio of 20. Error bars indicate 1σ uncertainties. The dashed line represents the ideal case in which the host flux is fully recovered.

A.2. *The effects of host SNR*

Our fiducial galaxy GN1034159 has a SNR > 10 in all bands, which is not the case for our full AGN sample. For the AGN galaxies in our sample with detected hosts, most have host S/N values above 3, with the exception of GN1086855 and GN1029154. In these two cases, although the host flux measured through aperture photometry has S/N < 3, the Sérsic model fluxes achieve S/N ~ 3. We therefore test the host-recovery behaviour under lower SNR conditions. To reduce the host SNR, we increase the noise in both the science image and its error map. We then repeat the entire procedure described above: we first fit the original images to obtain a Sérsic model for the host galaxy, and then inject scaled AGN (point source) models to generate mock images with different AGN/host flux ratios.

We find that as the host SNR decreases, the recovery degrades more quickly as the AGN/host flux ratio increases. In other words, the upper limit of the AGN/host ratio for which we can still recover the host flux reliably becomes lower as the host SNR is reduced. In the SW bands, the recovery remains robust even when the SNR is reduced to ~ 3. From F090W to F277W, the recovered host flux agrees with the true flux to within 20%, with fractional uncertainties $\lesssim 40\%$.

In contrast, the LW bands behave differently. In F356W, once the host SNR drops below ~ 3, the recovered flux becomes meaningless: the fractional uncertainty exceeds 150%, indicating that the measurement provides no useful constraint. In F444W, when the SNR falls below 5, the recovered host flux becomes $\sim$50% lower than the true value and the fractional uncertainty rises above $\sim$50%; we therefore treat these measurements as unreliable.

Overall, we find that as SNR decreases and as AGN/host ratio increases, the recovery becomes progressively worse. However, for SNR $\gtrsim 3$ and AGN/host ratios $\lesssim 1000$, the host flux can still be reliably recovered in the F090W–F277W bands (bias $< 20\%$, fractional uncertainty $< 40\%$). For F356W and F444W, the useful information is lost when the host SNR drops below $\sim$5 and $\sim$3, respectively.

What ultimately matters is whether the recovered fluxes allow us to obtain a reliable stellar-mass estimate. Running SED fits on the recovered fluxes for different SNR levels and AGN/host ratios, we find that as long as the AGN/host flux ratio is below $\sim$1000, the derived stellar mass differs from the true value (obtained from SED fits of the total flux of the original galaxy) by $\lesssim 0.5$ dex, even when the host SNR is as low as $\sim$3, as shown in Fig. 8.

We therefore conclude that when the host SNR is above 3 and the AGN/host ratio is smaller than 1000, the stellar mass can be recovered within 0.5 dex.

We also find that even when no AGN component is injected into the galaxy image, fitting the data with a PS+Sérsic model introduces a modest bias in the host flux. The recovered Sérsic flux is systematically deviated from the true total galaxy flux by $\sim 20\%$ (for SNR > 5 in F090W-F277W, the exact magnitude of the offset depending on both S/N and wavelength), corresponding to a typical stellar-mass bias of ≈ 0.2 dex. This systematic offset is therefore intrinsic to the PS+Sérsic decomposition, even in the absence of an AGN component.

A.3. *Sérsic Profile Recovery*

We tested the recovery of the Sérsic profile parameters under different injected AGN-to-host flux ratios to assess when reliable host-galaxy structural measurements can be obtained. For each ratio, we fit the mock images using GALFIT and take the Sérsic parameters recovered from the F115W band as the model of the host galaxy. Fig 9 shows how the recovered Sérsic parameters vary with flux ratio. The recovered parameters remain stable and consistent with the input model up to AGN-to-host ratios of <3 . At ratios of 5, the recovered parameters begin to deviate noticeably from the true values. At ratios of 15, GALFIT attempts to describe the source predominantly as a point source, yielding an unrealistically faint host magnitude ($\sim$32 mag). The estimated Sérsic parameters hit the boundaries we set and exhibit extremely large uncertainties, indicating that these fits are unreliable.

Based on our decomposition results, all targets in our sample with detected host emission have AGN-to-host flux ratios below 2. In this regime, we expect GALFIT to recover a reliable Sérsic profile for the host galaxy.

REFERENCES

Akins, H. B., Casey, C. M., Allen, N., et al. 2023, ApJ, 956, 61, doi: 10.3847/1538-4357/acef21

Akins, H. B., Casey, C. M., Berg, D. A., et al. 2025, ApJL, 980, L29, doi: 10.3847/2041-8213/adab76

Allen, N., Oesch, P. A., Toft, S., et al. 2025, A&A, 698, A30, doi: 10.1051/0004-6361/202452690

Baggen, J. F. W., van Dokkum, P., Brammer, G., et al. 2024, ApJL, 977, L13, doi: 10.3847/2041-8213/ad90b8

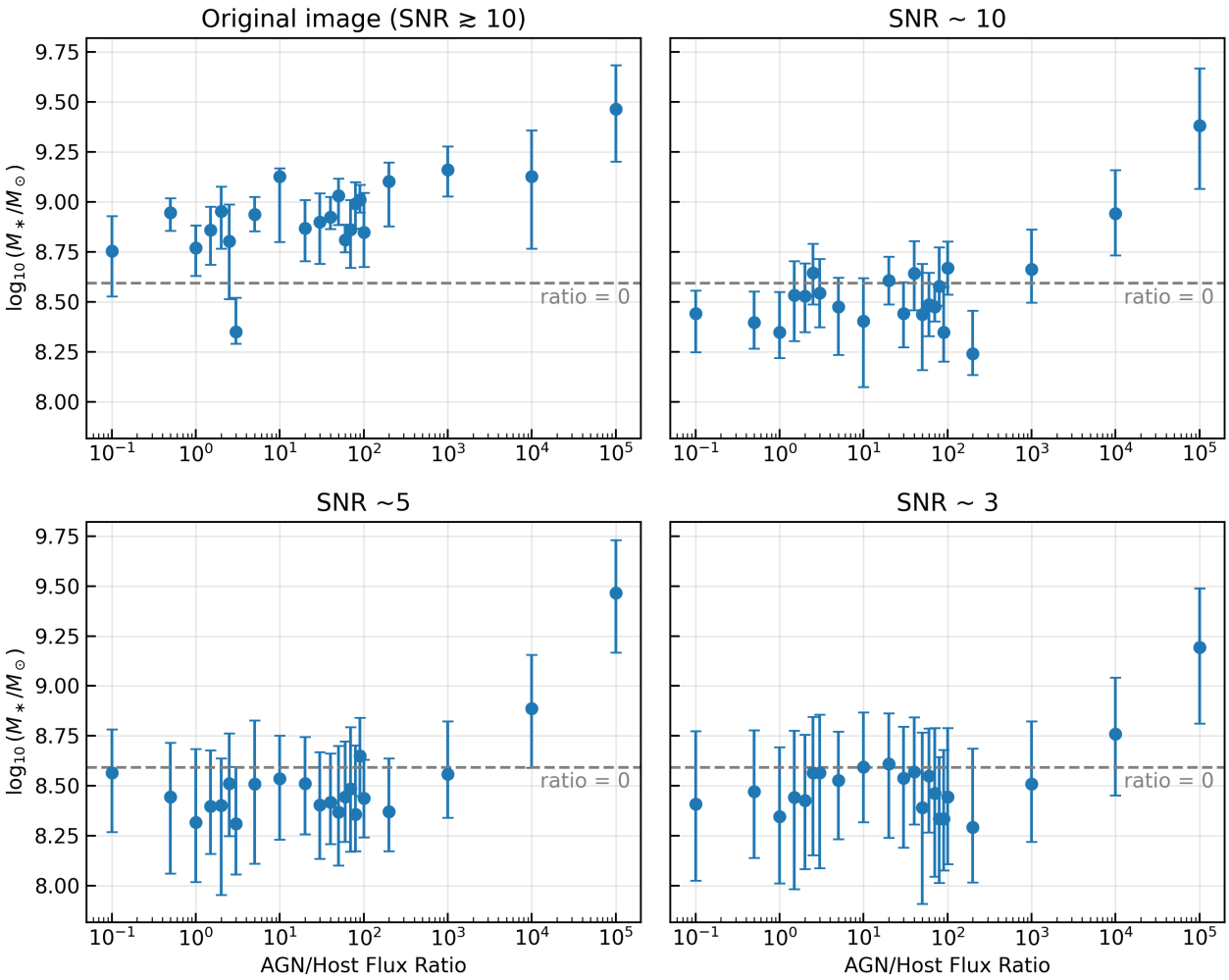

Figure 8. Stellar mass estimates as a function of the AGN-to-host flux ratio for simulated images at different SNRs, with 1 σ error bars. From top left to bottom right, the panels show results for the original image (SNR $\gtrsim$ 10), SNR $\sim$ 10, SNR $\sim$ 5, and SNR $\sim$ 3. The dashed line is the stellar mass estimate based on original input without AGN injection.

Baldwin, J. O., Nelson, E., Johnson, B. D., et al. 2024,, Astrophysics Source Code Library, record ascl:2410.006 http://ascl.net/2410.006

Barro, G., Pérez-González, P. G., Kocevski, D. D., et al. 2024, ApJ, 963, 128, doi: 10.3847/1538-4357/ad167e

Bogdán, Á., Goulding, A. D., Natarajan, P., et al. 2024, Nature Astronomy, 8, 126, doi: 10.1038/s41550-023-02111-9

Bunker, A. J., NIRSPEC Instrument Science Team, & JAESs Collaboration. 2020, in IAU Symposium, Vol. 352, Uncovering Early Galaxy Evolution in the ALMA and JWST Era, ed. E. da Cunha, J. Hodge, J. Afonso, L. Pentericci, & D. Sobral, 342–346, doi: 10.1017/S1743921319009463

Carreira, C., Robertson, B. E., Danhaive, A. L., et al. submitted, ApJ

Chen, C.-H., Ho, L. C., Li, R., & Inayoshi, K. 2025, ApJL, 989, L12, doi: 10.3847/2041-8213/adee0a

Chen, C.-H., Ho, L. C., Li, R., & Zhuang, M.-Y. 2024, arXiv e-prints, arXiv:2411.04446, doi: 10.48550/arXiv.2411.04446

Curtis-Lake, E., Cameron, A. J., Bunker, A. J., et al. 2025, arXiv e-prints, arXiv:2510.01033, doi: 10.48550/arXiv.2510.01033

Danhaive, A. L., Tacchella, S., McClymont, W., et al. 2025, arXiv e-prints, arXiv:2510.06315, doi: 10.48550/arXiv.2510.06315

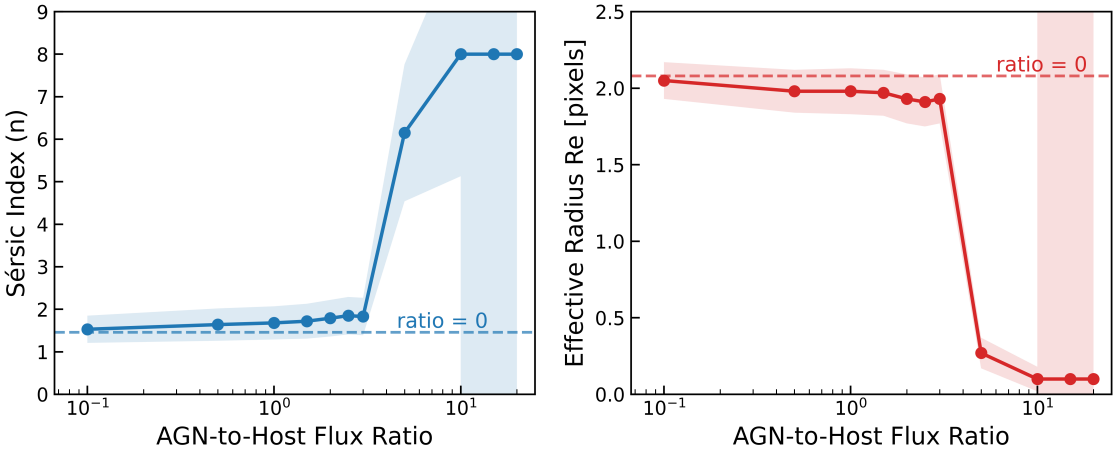

Figure 9. Sérsic parameter recovery as a function of AGN-to-host flux ratio in the F115W band. The left panel shows the recovered Sérsic index n, and the right panel shows the effective radius R_e in pixels, both derived from the GALFIT decomposition of mock AGN–host images. The Sérsic parameters obtained from the original galaxy image (with no injected AGN component) are shown as dashed lines. The shaded regions indicate the 1σ uncertainties reported by GALFIT.

de Graaff, A., Hviding, R. E., Naidu, R. P., et al. 2025, arXiv e-prints, arXiv:2511.21820, doi: 10.48550/arXiv.2511.21820

D'Eugenio, F., Cameron, A. J., Scholtz, J., et al. 2025a, ApJS, 277, 4, doi: 10.3847/1538-4365/ada148

D'Eugenio, F., Maiolino, R., Perna, M., et al. 2025b, arXiv e-prints, arXiv:2503.11752, doi: 10.48550/arXiv.2503.11752

Ding, X., Onoue, M., Silverman, J. D., et al. 2023, Nature, 621, 51, doi: 10.1038/s41586-023-06345-5

Fabian, A. C. 2012, ARA&A, 50, 455, doi: 10.1146/annurev-astro-081811-125521

Fan, X., Bañados, E., & Simcoe, R. A. 2023, ARA&A, 61, 373, doi: 10.1146/annurev-astro-052920-102455

Ferrarese, L., & Merritt, D. 2000, ApJL, 539, L9, doi: 10.1086/312838

Fujimoto, S., Ouchi, M., Kohno, K., et al. 2024, arXiv e-prints, arXiv:2402.18543, doi: 10.48550/arXiv.2402.18543

Furtak, L. J., Labbé, I., Zitrin, A., et al. 2024, Nature, 628, 57, doi: 10.1038/s41586-024-07184-8

Furtak, L. J., Secunda, A. R., Greene, J. E., et al. 2025, A&A, 698, A227, doi: 10.1051/0004-6361/202554110

Gebhardt, K., Bender, R., Bower, G., et al. 2000, ApJL, 539, L13, doi: 10.1086/312840

Geris, S., Maiolino, R., Isobe, Y., et al. 2026, MNRAS, 545, staf1979, doi: 10.1093/mnras/staf1979

Goulding, A. D., Greene, J. E., Setton, D. J., et al. 2023, ApJL, 955, L24, doi: 10.3847/2041-8213/acf7c5

Greene, J. E., Strader, J., & Ho, L. C. 2020, ARA&A, 58, 257, doi: 10.1146/annurev-astro-032620-021835

Greene, J. E., Labbe, I., Goulding, A. D., et al. 2024, ApJ, 964, 39, doi: 10.3847/1538-4357/ad1e5f

Hainline, K. N., Maiolino, R., Juodžbalis, I., et al. 2025, ApJ, 979, 138, doi: 10.3847/1538-4357/ad9920

Harikane, Y., Zhang, Y., Nakajima, K., et al. 2023, ApJ, 959, 39, doi: 10.3847/1538-4357/ad029e

Hausen, R., & Robertson, B. E. 2022, Astronomy and Computing, 39, 100586, doi: 10.1016/j.ascom.2022.100586

Huertas-Company, M., Iyer, K. G., Angeloudi, E., et al. 2024, A&A, 685, A48, doi: 10.1051/0004-6361/202346800

Inayoshi, K., & Maiolino, R. 2025, ApJL, 980, L27, doi: 10.3847/2041-8213/adaebd

Ji, X., Maiolino, R., Übler, H., et al. 2025, MNRAS, 544, 3900, doi: 10.1093/mnras/staf1867

Ji, Z., Williams, C. C., Tacchella, S., et al. 2024, ApJ, 974, 135, doi: 10.3847/1538-4357/ad6e7f

Johnson, B. D., Leja, J., Conroy, C., & Speagle, J. S. 2021, The Astrophysical Journal Supplement Series, 254, 22, doi: 10.3847/1538-4365/abef67

Johnson, B. D., Robertson, B. E., Eisenstein, D. J., et al. submitted, ApJ

Jones, B. L., Kocevski, D. D., Pacucci, F., et al. 2025, arXiv e-prints, arXiv:2510.07376, doi: 10.48550/arXiv.2510.07376

Juodžbalis, I., Maiolino, R., Baker, W. M., et al. 2024, Nature, 636, 594, doi: 10.1038/s41586-024-08210-5

Juodžbalis, I., Maiolino, R., Baker, W. M., et al. 2025a, arXiv e-prints, arXiv:2504.03551, doi: 10.48550/arXiv.2504.03551

Juodžbalis, I., Marconcini, C., D'Eugenio, F., et al. 2025b, arXiv e-prints, arXiv:2508.21748, doi: 10.48550/arXiv.2508.21748

Kennedy, R., Bamford, S. P., Baldry, I., et al. 2015, MNRAS, 454, 806, doi: 10.1093/mnras/stv2032

Kocevski, D. D., Onoue, M., Inayoshi, K., et al. 2023, ApJL, 954, L4, doi: 10.3847/2041-8213/ace5a0

Kokorev, V., Caputi, K. I., Greene, J. E., et al. 2024, ApJ, 968, 38, doi: 10.3847/1538-4357/ad4265

Kormendy, J., & Ho, L. C. 2013, ARA&A, 51, 511, doi: 10.1146/annurev-astro-082708-101811

Labbe, I., Greene, J. E., Bezanson, R., et al. 2025, ApJ, 978, 92, doi: 10.3847/1538-4357/ad3551

Larson, R. L., Finkelstein, S. L., Kocevski, D. D., et al. 2023, ApJL, 953, L29, doi: 10.3847/2041-8213/ace619

Lin, X., Fan, X., Cai, Z., et al. 2025, arXiv e-prints, arXiv:2507.10659, doi: 10.48550/arXiv.2507.10659

Lyu, J., Alberts, S., Rieke, G. H., et al. 2024, ApJ, 966, 229, doi: 10.3847/1538-4357/ad3643

Magorrian, J., Tremaine, S., Richstone, D., et al. 1998, AJ, 115, 2285, doi: 10.1086/300353

Maiolino, R., Scholtz, J., Curtis-Lake, E., et al. 2024, A&A, 691, A145, doi: 10.1051/0004-6361/202347640

Maiolino, R., Risaliti, G., Signorini, M., et al. 2025, MNRAS, 538, 1921, doi: 10.1093/mnras/staf359

Marshall, M. A., Windhorst, R. A., Ferrami, G., et al. 2025, A&A, 702, A174, doi: 10.1051/0004-6361/202554307

Mathews, E. P., Leja, J., Speagle, J. S., et al. 2023, The Astrophysical Journal, 954, 132, doi: 10.3847/1538-4357/ace720

Matthee, J., Naidu, R. P., Brammer, G., et al. 2024, ApJ, 963, 129, doi: 10.3847/1538-4357/ad2345

Naidu, R. P., Matthee, J., Katz, H., et al. 2025, arXiv e-prints, arXiv:2503.16596, doi: 10.48550/arXiv.2503.16596

Natarajan, P., Pacucci, F., Ricarte, A., et al. 2024, ApJL, 960, L1, doi: 10.3847/2041-8213/ad0e76

Oesch, P. A., Brammer, G., Naidu, R. P., et al. 2023, MNRAS, 525, 2864, doi: 10.1093/mnras/stad2411

Oke, J. B., & Gunn, J. E. 1983, ApJ, 266, 713, doi: 10.1086/160817

Peng, C. Y. 2007, ApJ, 671, 1098, doi: 10.1086/522774

Peng, C. Y., Ho, L. C., Impey, C. D., & Rix, H.-W. 2002, AJ, 124, 266, doi: 10.1086/340952

Peng, C. Y., Ho, L. C., Impey, C. D., & Rix, H.-W. 2010, AJ, 139, 2097, doi: 10.1088/0004-6256/139/6/2097

Pérez-González, P. G., Barro, G., Rieke, G. H., et al. 2024, ApJ, 968, 4, doi: 10.3847/1538-4357/ad38bb

Perrin, M. D., Sivaramakrishnan, A., Lajoie, C.-P., et al. 2014, in Society of Photo-Optical Instrumentation Engineers (SPIE) Conference Series, Vol. 9143, Space Telescopes and Instrumentation 2014: Optical, Infrared, and Millimeter Wave, ed. J. M. Oschmann, Jr., M. Clampin, G. G. Fazio, & H. A. MacEwen, 91433X, doi: 10.1117/12.2056689

Reines, A. E., Greene, J. E., & Geha, M. 2013, ApJ, 775, 116, doi: 10.1088/0004-637X/775/2/116

Reines, A. E., & Volonteri, M. 2015, ApJ, 813, 82, doi: 10.1088/0004-637X/813/2/82

Rinaldi, P., Bonaventura, N., Rieke, G. H., et al. 2025a, ApJ, 992, 71, doi: 10.3847/1538-4357/adfa10

Rinaldi, P., Rieke, G. H., Wu, Z., et al. 2025b, arXiv e-prints, arXiv:2507.17738, doi: 10.48550/arXiv.2507.17738

Robertson, B. E., Johnson, B. D., Tacchella, S., et al. submitted, ApJ

Rusakov, V., Watson, D., Nikopoulos, G. P., et al. 2025, arXiv e-prints, arXiv:2503.16595, doi: 10.48550/arXiv.2503.16595

Scholtz, J., Carniani, S., Parlanti, E., et al. 2025, arXiv e-prints, arXiv:2510.01034, doi: 10.48550/arXiv.2510.01034

Sharma, R. S., Choi, E., Somerville, R. S., et al. 2024, MNRAS, 527, 9461, doi: 10.1093/mnras/stad3836

Somerville, R. S., Hopkins, P. F., Cox, T. J., Robertson, B. E., & Hernquist, L. 2008, MNRAS, 391, 481, doi: 10.1111/j.1365-2966.2008.13805.x

Stone, M. A., Lyu, J., Rieke, G. H., & Alberts, S. 2023, ApJ, 953, 180, doi: 10.3847/1538-4357/acebe0

Sun, Y., Rieke, G. H., Lyu, J., et al. 2025, ApJ, 983, 165, doi: 10.3847/1538-4357/adc250

Trakhtenbrot, B., Netzer, H., Lira, P., & Shemmer, O. 2011, ApJ, 730, 7, doi: 10.1088/0004-637X/730/1/7

Übler, H., Maiolino, R., Curtis-Lake, E., et al. 2023, A&A, 677, A145, doi: 10.1051/0004-6361/202346137

Vulcani, B., Bamford, S. P., Häußler, B., et al. 2014, MNRAS, 441, 1340, doi: 10.1093/mnras/stu632

Wang, T., Sun, H., Zhou, L., et al. 2025, ApJL, 988, L35, doi: 10.3847/2041-8213/adebe7

Williams, C. C., Alberts, S., Ji, Z., et al. 2024, ApJ, 968, 34, doi: 10.3847/1538-4357/ad3f17

Yu, H., Fan, L., Han, Y., et al. 2025, ApJ, 978, 164, doi: 10.3847/1538-4357/ad9aa3

Yue, M., Eilers, A.-C., Simcoe, R. A., et al. 2024, ApJ, 966, 176, doi: 10.3847/1538-4357/ad3914

Zhang, J., Egami, E., Sun, F., et al. 2025, arXiv e-prints, arXiv:2505.02895, doi: 10.48550/arXiv.2505.02895

Zhu, Y., Alberts, S., Lyu, J., et al. 2024, arXiv e-prints, arXiv:2410.14804, doi: 10.48550/arXiv.2410.14804

Zhuang, M.-Y., Li, J., & Shen, Y. 2024, ApJ, 962, 93, doi: 10.3847/1538-4357/ad1517